Available online at www.sciencedirect.com
ScienceDirect
Trans. Nonferrous Met. Soc. China 31(2021) 533−544
Transactions of Nonferrous Metals Society of China
www.tnmsc.cn

Construction of $BiVO_4$ nanosheets@WO_3 arrays heterojunction photoanodes by versatile phase transformation strategy

Xin SU[1], Can-jun LIU[1], Yang LIU[2], Ya-hui YANG[3], Xuan LIU[1], Shu CHEN[1]

1. Key Laboratory of Theoretical Organic Chemistry and Function Molecule of Ministry of Education, School of Chemistry and Chemical Engineering, Hunan University of Science and Technology, Xiangtan 411201, China;
2. School of Chemistry and Chemical Engineering, Central South University, Changsha 410083, China;
3. School of Chemistry and Chemical Engineering, Hunan Normal University, Changsha 410081, China

Received 12 March 2020; accepted 21 December 2020

Abstract: A versatile phase transformation strategy was proposed to synthesize novel $BiVO_4$ nanosheets (NSs)@WO_3 nanorod (NR) and nanoplate (NP) arrays films. The strategy was carried out by following a three-step hydrothermal process (WO_3→WO_3/Bi_2WO_6→$WO_3/BiVO_4$). According to the characterization results, plenty of $BiVO_4$ NSs grew well on the surface of WO_3 NR and NP arrays films, thus forming the $WO_3/BiVO_4$ heterojunction structure. The prepared $WO_3/BiVO_4$ heterojunction films were used as the photoanodes for the photoelectrochemical (PEC) water splitting. As indicated by the results, the photoanodes exhibited an excellent PEC activity. The photocurrent densities of the $WO_3/BiVO_4$ NR and NP photoanodes at 1.23 V (vs RHE) without cocatalyst under visible light illumination reached up to about 1.56 and 1.20 mA/cm^2, respectively.

Key words: photoanode; bismuth vanadate; tungsten oxide; heterojunction

1 Introduction

The renewable generation of the clean fuels plays an essential role in meeting the growing demand for the energy and reversing environmental deterioration [1,2]. Photoelectrochemical (PEC) water splitting is potentially an ideal approach to obtaining hydrogen fuels directly from sunlight [3]. Since the first report on TiO_2 film photoanode in 1972 [4], plenty of efforts have been devoted to developing a high-efficiency photoanode for PEC water splitting over the past decades [5]. Up to now, some semiconductor materials have been applied as photoanodes, such as ZnO [6], Fe_2O_3 [7], WO_3 [8], TiO_2 [9] and $BiVO_4$ [10].

Especially, WO_3 is widely recognized as a promising photoanode material for its nontoxicity, high electrochemical stability and excellent charge-transferring ability [11]. However, the solar-to-hydrogen efficiency (STHE) of single WO_3 photoanode is low due to its poor ability to absorb visible light and the high recombination rate of photogenerated carriers [12]. Thus, some strategies have been proposed to address these issues, including morphology control [13], element doping [14], and heterojunction constructing [15], etc. Particularly, the construction of heterojunction with other narrow-gap semiconductors has been confirmed as an effective method in promoting the spatial separation of photogenerated carriers and extending the visible-light response simultaneously.

As a narrow-gap semiconductor, $BiVO_4$ is considered to be one of the most promising materials fit for the construction of type-II alignment heterojunction with WO_3, due to its

Corresponding author: Can-jun LIU, Tel: +86-15073161782, E-mail: liucanjun@hnust.edu.cn; Shu CHEN, E-mail: chenshu@hnust.edu.cn
DOI: 10.1016/S1003-6326(21)65515-2
1003-6326/© 2021 The Nonferrous Metals Society of China. Published by Elsevier Ltd & Science Press

excellent performance in absorbing visible light ($\lambda \leq 520$ nm), high chemical stability and desirable conduction band (CB) position [16,17]. Therefore, $WO_3/BiVO_4$ films as photoanodes have been extensively studied [18]. Applying a solvothermal technique, SU et al [19] prepared a novel $WO_3/BiVO_4$ nanorod (NR) arrays photoanode that achieved a higher PEC activity than the planar $WO_3/BiVO_4$ photoanode. SHI et al [20] constructed a $WO_3/BiVO_4$ helix nanostructure heterojunction that demonstrated such advantages as effective light scattering, large contact surface area as well as high rate of carriers separation and transportation. Besides, its performance was verified through theoretical simulation and analysis. LEE et al [21] prepared a 1D $WO_3/BiVO_4$ photoanode by depositing dot-like $BiVO_4$ on the WO_3 NR surface. A systematic analysis was conducted to reveal the vital role played by the optimization of WO_3 NR morphology in achieving high PEC efficiency. According to the aforementioned studies, the morphology and nanostructure of $WO_3/BiVO_4$ heterojunction play a significant role in improving the PEC efficiency.

Recently, an in-situ transformation method has been widely applied to constructing heterostructure. Taking a anion transformation approach, GAO et al [22] prepared novel $BiVO_4/Bi_2S_3$ hollow nano-discoidals that exhibited superior photocatalytic activity. CHITRADA et al [23] produced Bi_2O_3−BiO_{2-x} photoanode using the in-situ photo-conversion method and the formation of photo-converted Bi_2O_{4-x} phase was conducive to absorbing more visible light, thus leading to high photocurrent density. The in-situ transformation method is considered to be more effortless to adjust the morphology and nanostructure of heterostructure compared with other methods. Besides, the heterostructure constructed using this method shows a reduced interface defect [24]. Thus, it is necessary to develop an in-situ transformation to prepare $WO_3/BiVO_4$ heterojunctions with various morphologies and study their PEC performance.

In this study, a versatile phase transformation strategy was applied to designing and fabricating novel $BiVO_4$ NS@WO_3 NR and NP arrays photoanodes. The strategy was performed via a three-step hydrothermal process ($WO_3 \rightarrow WO_3/Bi_2WO_6 \rightarrow WO_3/BiVO_4$). The morphology and nanostructure of samples prepared by the strategy were characterized and the corresponding PEC properties were investigated.

2 Experimental

2.1 Synthesis of WO_3 NR and NP arrays on FTO substrate

WO_3 NR arrays were prepared using a hydrothermal method as described in the previous reports [25]. Firstly, 0.15 g of ammonium paratungstate was dissolved in 15 mL of deionized water. Then, 0.6 mL of 12 mol/L HCl and 0.3 mL of H_2O_2 were added in sequence into the above-mentioned aqueous solution by stirring. Then, an FTO substrate was immersed in 20 mL of Teflon-lined autoclave and placed against the wall with the conductive side downward. Subsequently, the aforementioned precursor solution was poured into the autoclave and the hydrothermal process was conducted at 170 °C for 4 h. Finally, the obtained films were annealed at 300 °C for 1 h before further use.

WO_3 NP arrays were synthesized using a hydrothermal method as described in the previous reports [26]. Firstly, 0.25 g of $Na_2WO_4 \cdot 2H_2O$ was added into 30 mL of deionized water by stirring. Then, 6 mL of 3 mol/L HCl, 30 mL of deionized water and 0.20 g of $(NH_4)_2C_2O_4$ were added into the aforementioned solution and stirred for 30 min. Then, an FTO substrate was immersed in 100 mL of Teflon-lined autoclave and placed against the wall with the conductive side downward. Afterwards, the above-mentioned precursor solution was poured into the autoclave and the hydrothermal process was conducted at 140 °C for 6 h. Finally, the obtained films were annealed at 300 °C for 1 h before further use.

2.2 Synthesis of WO_3/Bi_2WO_6 NR and NP arrays on FTO substrate

The WO_3/Bi_2WO_6 films were prepared through hydrothermal treatment. Firstly, the hydrothermal reaction solution was obtained by adding 0.6 g of $Bi(NO_3)_3 \cdot 5H_2O$ as the Bi source into 30 mL of 0.2 mol/L HNO_3 solution. Then, the WO_3 NR or WO_3 NP arrays films were immersed in 50 mL of Teflon-lined autoclave and placed against the wall

with the sample side facing down. Then, the aforementioned precursor solution was poured into the autoclave and the hydrothermal process was conducted at 200 °C for 10 h. Finally, the obtained films were annealed at 540 °C for 4 h before further use.

2.3 Synthesis of $WO_3/BiVO_4$ NR and NP arrays on FTO substrate

The $WO_3/BiVO_4$ films were prepared through hydrothermal treatment. Firstly, the precursor solution was prepared by adding 4 mg of NH_4VO_3 and 0.2 mL of 3 mol/L HCl into 30 mL of deionized water. Then, the WO_3/Bi_2WO_6 films were immersed in 50 mL of Teflon-lined autoclave and placed against the wall with the sample side facing down. Then, the above-mentioned solution was transferred into the autoclave and placed in an oven at 180 °C for 4 h. Subsequent to the reaction, the formed films were calcined at 500 °C for 1 h before further use.

2.4 Characterization

The crystal, morphological and optical characteristics were examined using X-ray diffractometer (XRD, D8 Advance, AXS), transmission electron microscope (TEM, Titan G2 60-300, FEI), field emission scanning electron microscope (FE-SEM, MIRA3, TESCAN) and UV-vis spectrophotometer (UV-vis, 2450, Shimadzu).

2.5 PEC measurement

The PEC measurements were performed in a three-electrode PEC cell on an electrochemical workstation (Zahner, Zennium, Germany). 0.5 mol/L of KH_2PO_4 (pH≈4.1) was treated as the electrolyte. A 500 W Xe lamp (CHF-XM, Perfectlight) coupled with a 400 nm cutoff filter was applied as the light source and the light intensity at the photoanode position was adjusted to 100 mW/cm^2, as measured using a light power meter (PL-MW2000, Perfectlight). The electrochemical impedance spectra (EIS) were recorded at 1.23 V (vs RHE) with a frequency of 10^4−0.1 Hz.

3 Results and discussion

3.1 Microstructure

$WO_3/BiVO_4$ arrays heterojunction films were fabricated using a three-step hydrothermal strategy and the fabrication process is illustrated in Fig. 1. The WO_3 NR and NP arrays films were initially prepared according to the previous reports [25,26]. Subsequently, the Bi_2WO_6 NS developed on the surface of WO_3 NR and NP arrays films under hydrothermal conditions as a result of the chemical reaction is shown as

$$2Bi^{3+}+WO_3+3H_2O \rightarrow Bi_2WO_6+6H^+ \quad (1)$$

Finally, Bi_2WO_6 NS was transformed into $BiVO_4$ NS on the surface of WO_3 to obtain $BiVO_4$ NS@WO_3 arrays films. The potential reaction is expressed as

$$Bi_2WO_6+2VO_3^- \rightarrow 2BiVO_4+WO_4^{2-} \quad (2)$$

The microstructure and morphology of the samples were characterized using SEM and TEM. According to the SEM images of the WO_3 NR (Figs. 2(a, b)) and NP (Figs. 2(g, h)) arrays films, both WO_3 NR and NP had vertically grown on the FTO substrate after the hydrothermal treatment and their surface was smooth. As shown in the cross-sectional view images, the length of WO_3 NR is approximately 2.5 μm and WO_3 NP ranges from 0.5 to 1 μm in edge length and from 80 to 200 nm in thickness. After the second-step hydrothermal

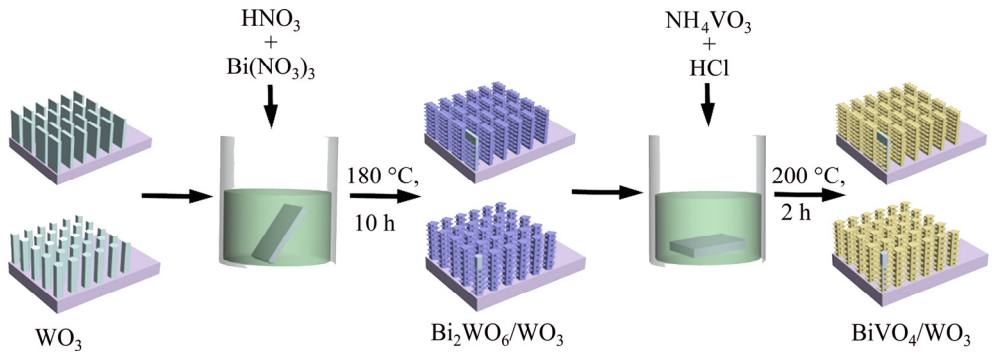

Fig. 1 Schematic illustration of preparation process for $WO_3/BiVO_4$ NR and NP arrays films

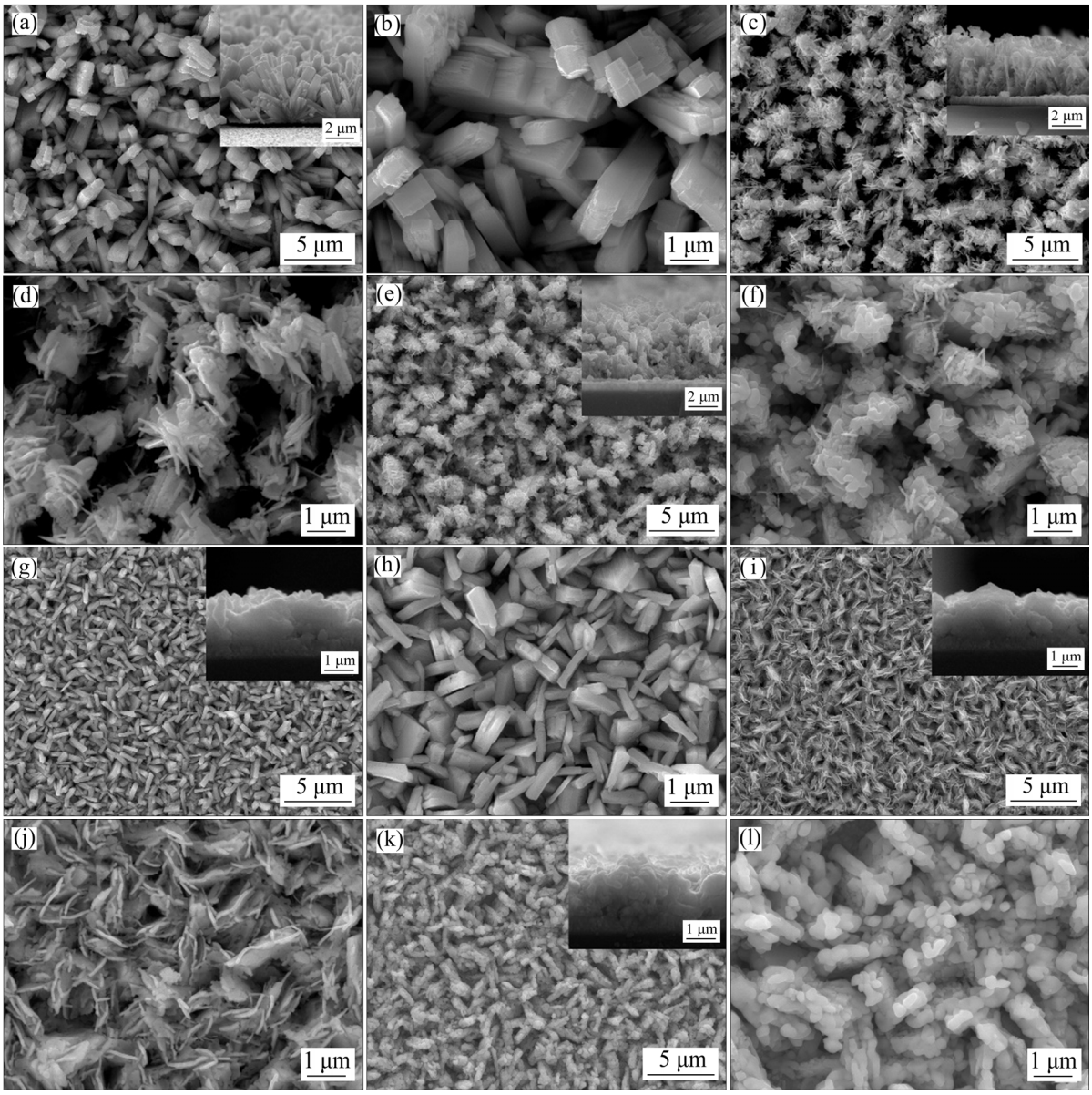

Fig. 2 SEM images of WO_3 NR (a, b), WO_3/Bi_2WO_6 NR (c, d), $WO_3/BiVO_4$ NR (e, f), WO_3 NP (g, h), WO_3/Bi_2WO_6 NP (i, j) and $WO_3/BiVO_4$ NP (k, l) arrays films

treatment, the surface of WO_3 NR and NP was rough and plenty of Bi_2WO_6 NS has epitaxially grown on the WO_3 surface, thus leading to the generation of WO_3/Bi_2WO_6 NR (Figs. 2(c, d)) and NP (Figs. 2(i, j)) films, which is attributed to the in-situ formation of Bi_2WO_6 NS as a result of the reaction occurring between WO_3 and Bi^{3+} under hydrothermal conditions. As shown in Figs. 2(e, f) and Figs. 2(k, l), there are some small NSs adhering on the surface of WO_3 NR and NP, because the Bi_2WO_6 NS on the WO_3 surface could be transformed into $BiVO_4$ NS by the third-step hydrothermal treatment, indicating the formation of $WO_3/BiVO_4$ NR and NP heterojunction films.

According to the TEM images of $WO_3/BiVO_4$ NR (Figs. 3(a−c)) and NP (Figs. 3(d−f)), WO_3 NR has a rod-like nanostructure and WO_3 NP possesses a plate-like nanostructure, which is consistent with the SEM images. As shown in LRTEM image, the surfaces of WO_3 NR and NP are covered with a large number of NSs. According to the HRTEM images, NS exhibits clear lattice fringes with spacings of 0.260 and 0.254 nm, which are consistent with the (200) and (020) crystal planes of monoclinic $BiVO_4$, respectively. By contrast, the NP shows a lattice spacing of 0.335 nm, corresponding to the (120) crystal plane of the monoclinic WO_3.

Furthermore, as suggested by the elemental mappings of $WO_3/BiVO_4$ NR (Fig. 4(a)) and NP (Fig. 4(b)), W, V and Bi elements are distributed uniformly, indicating the formation of $BiVO_4$ NS@WO_3 arrays heterojunction films.

The phase and crystallinity of WO_3, WO_3/Bi_2WO_6 and $WO_3/BiVO_4$ films were characterized by XRD, as shown in Figs. 5(a, b). The obtained WO_3 arrays films exhibit the characteristic diffraction peaks of monoclinic WO_3 (JCPDS 83-0950). As for the WO_3/Bi_2WO_6 films, the observed peaks of characteristic diffraction at 28.31° and 32.93° are assigned to the (113) and (020) crystal planes of orthorhombic Bi_2WO_6 (JCPDS 73-2020), respectively. Corresponding to the (011), (112) and (004) crystal planes of

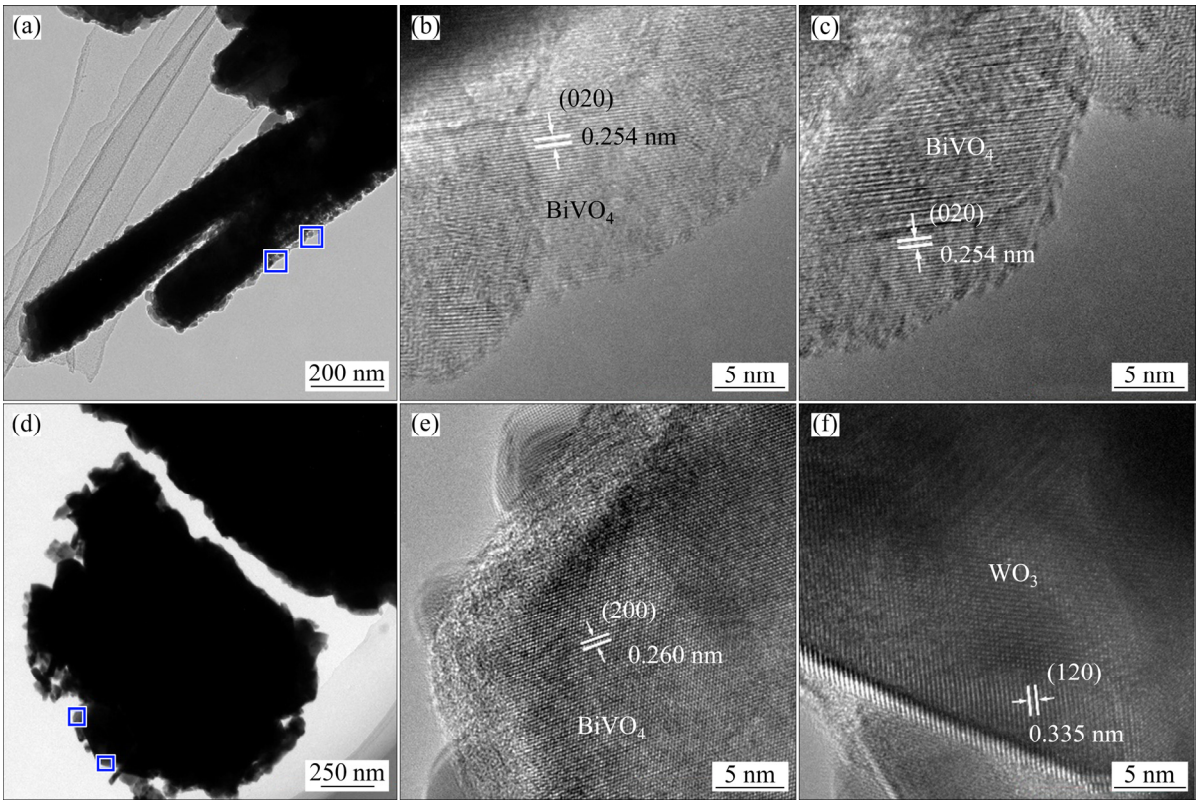

Fig. 3 TEM images of $WO_3/BiVO_4$ NR (a−c) and NP (d−f)

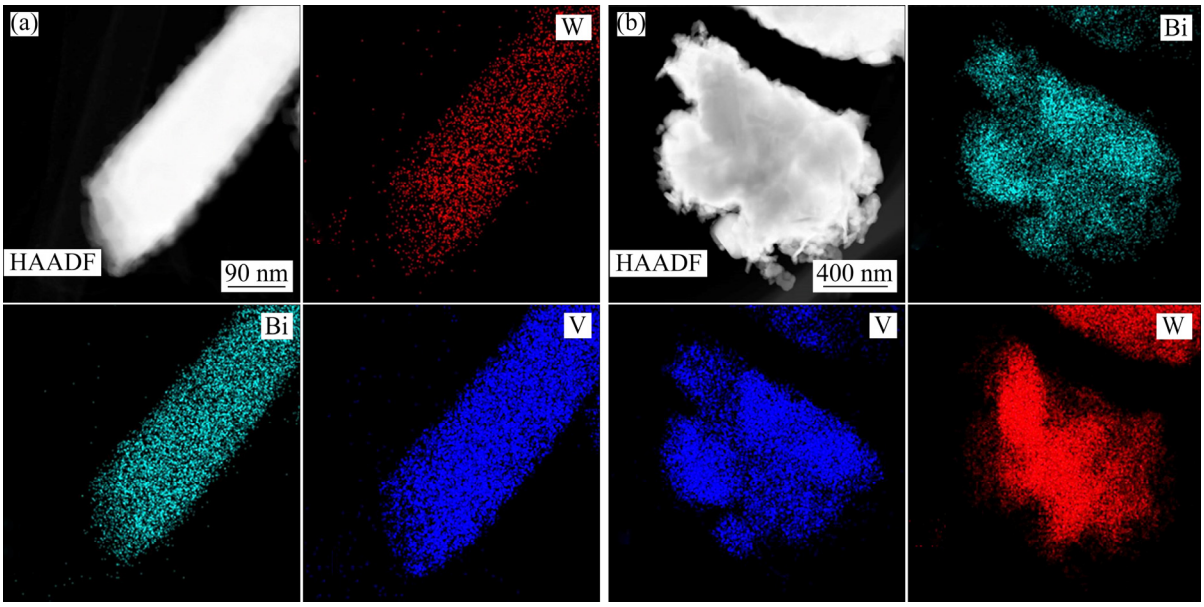

Fig. 4 Elemental mapping images of $WO_3/BiVO_4$ NR (a) and NP (b)

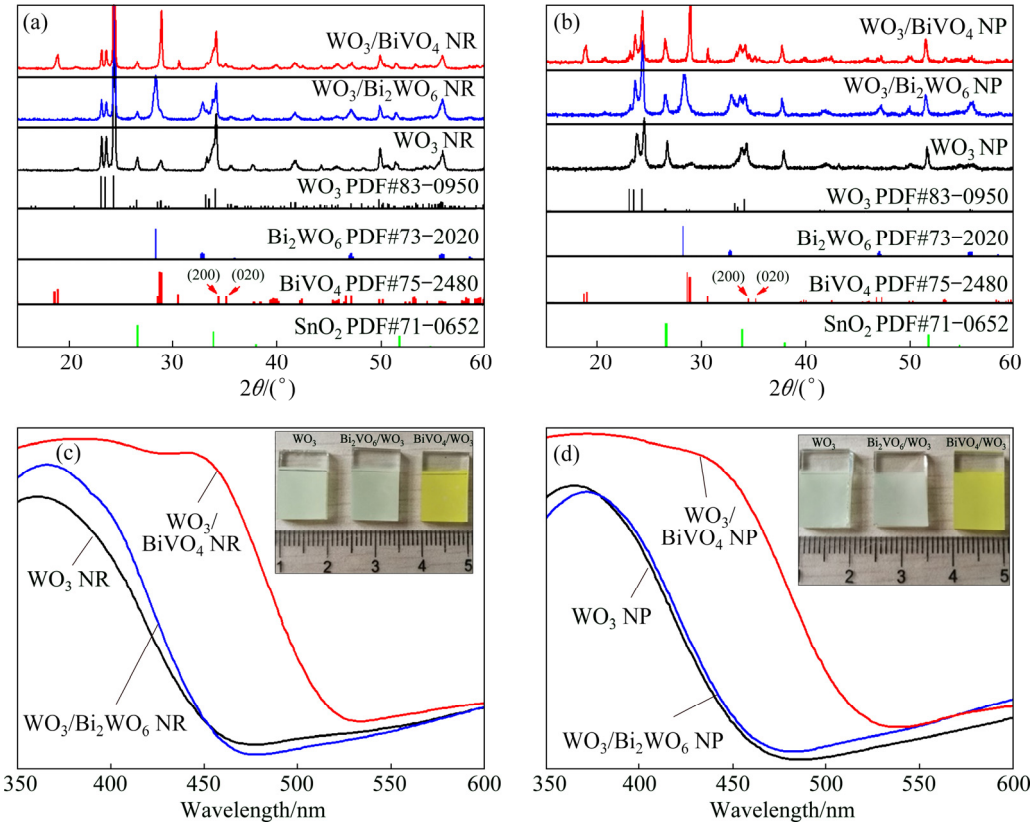

Fig. 5 XRD patterns (a, b) and UV-vis absorption spectra (c, d) of prepared film

monoclinic $BiVO_4$, new peaks observed at 18.98°, 28.95° and 30.53° are distinguishable from the XRD patterns of $WO_3/BiVO_4$ films (JCPDS 75-2480), suggesting the formation of $BiVO_4$ on the surface of WO_3 films. Figures 5 shows the spectra of UV-vis absorption. The optical absorption of WO_3 films shows similarity to WO_3/Bi_2WO_6 films, with the edges of their absorption being around 470 nm, which corresponds to their bandgap energy (E_g≈2.7 eV). In addition, $WO_3/BiVO_4$ films show a visible redshift and their absorption edges are about 520 nm, which is consistent with the bandgap energy of $BiVO_4$ (E_g≈2.4 eV). As a result, the absorption of visible light by the films can be improved significantly by the formation of $BiVO_4$ on the surface of WO_3. As shown in Figs. 5(c, d), the images of the prepared films also are consistent with the UV-vis absorption results. WO_3 NR and NP films are yellow−green while $WO_3/BiVO_4$ films are bright yellow.

3.2 PEC performance of $WO_3/BiVO_4$ photoanodes

In order to assess the PEC performance, the chopped linear sweep voltammetry (LSV) plots were obtained in 0.5 mol/L KH_2PO_4 electrolyte under visible light. As shown in Figs. 6(a, b), the photocurrent density of the $WO_3/BiVO_4$ NR and NP photoanodes is significantly improved after the formation of $BiVO_4$ on the surface of WO_3 arrays. The photocurrent densities of $WO_3/BiVO_4$ NR and NP photoanodes reach ca. 1.56 and 1.21 mA/cm^2 at 1.23 V (vs RHE), respectively, which are much higher compared with pure WO_3 NR and NP photoanodes. More importantly, the photocurrent density and onset potential of the prepared $WO_3/BiVO_4$ photoanodes are comparable to the reported $WO_3/BiVO_4$ photoanodes without cocatalysts, as indicated in Table 1.

In this study, the incident photon-to-electron conversion efficiency (IPCE) was examined to figure out the relationship between photocurrent density and light absorption. The IPCE plots were recorded at a constant potential of 1.23 V(vs RHE), as shown in Figs. 6(c, d). It can be seen that $WO_3/BiVO_4$ NR and NP photoanodes achieve the highest IPCE value in the overall wavelength range due to the type-II heterojunction structure of the $WO_3/BiVO_4$ photoanodes, which is conducive to the separation and transfer of photogenerated

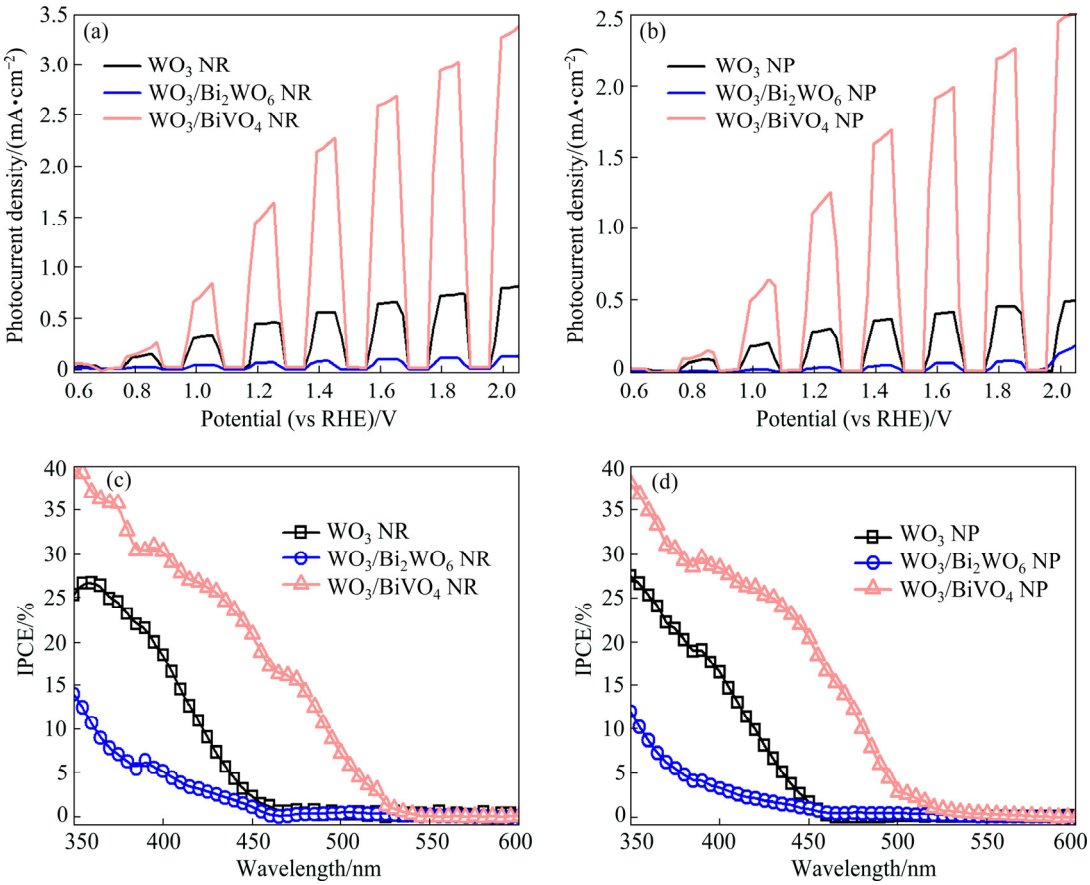

Fig. 6 LSV plots (a, b) and IPCE spectra (c, d) of as-prepared photoanode

Table 1 PEC performance of $WO_3/BiVO_4$ photoanode without cocatalyst in previous literatures

Morphology	Electrolyte	Potential/V	Photocurrent density/(mA·cm^{-2})	Onset potential/V	Ref.
Nanoporous	Na_2SO_4	0.7 (vs Ag/AgCl)	1.74	−0.15 (vs Ag/AgCl)	[27]
Nanorod arrays	Na_2SO_4	1 (vs NHE)	1.6	About −0.4 (vs NHE)	[19]
Nanoporous	KH_2PO_4	0.6 (vs Ag/AgCl)	2.01	About −0.1 (vs Ag/AgCl)	[28]
Nanoporous	KPi	1.23 (vs RHE)	0.84	About 0 (vs Ag/AgCl)	[29]
Nanoporous	Na_2SO_4	1.23 (vs RHE)	1.01	About 0.3 (vs RHE)	[30]
Nanoplate arrays	Na_2SO_4	1.23 (vs RHE)	About 1.62	About 0.4 (vs RHE)	[31]
Nanofiber	Na_2SO_4	1.23 (vs RHE)	1.31	About 0.3 (vs RHE)	[32]
Nanoplate arrays	KH_2PO_4	1.23 (vs RHE)	1.21	About 0.45 (vs RHE)	This work
Nanorod arrays	KH_2PO_4	1.23 (vs RHE)	1.56	About 0.4 (vs RHE)	This work

KPi is phosphate buffer solution at pH 7.

charge carriers. Furthermore, $WO_3/BiVO_4$ photoanodes show an extended photo-responsive range (~520 nm) due to the narrower bandgap energy of $BiVO_4$.

To evaluate the ability of charge transfer, the EIS of the photoanodes was measured within the frequency range of 10^4–10^{-1} Hz at 1.23 V (vs RHE) under visible light, as shown in Fig. 7. All photoanodes show a single semicircle, suggesting that the charge transfer across the photoelectrode/electrolyte interface is the only rate-limiting step. Compared with the WO_3 and WO_3/Bi_2WO_6 photoanodes, $WO_3/BiVO_4$ photoanodes exhibit a smaller arc radius, indicating the better performance achieved by $WO_3/BiVO_4$ photoanode in interfacial charge transfer.

In addition, the EIS data are fitted by the equivalent circuit consisting of a solution resistance (R_s), a charge transfer resistance (R_1) and a constant phase element (CPE_1), as shown in the inset in Fig. 7. As indicated by the fitted results listed in Table 2, $WO_3/BiVO_4$ photoanodes have the smallest

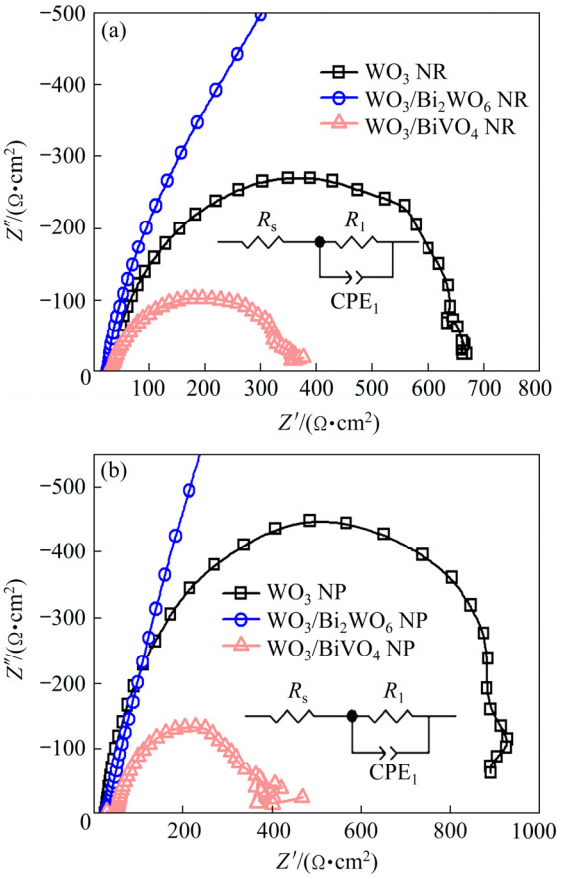

Fig. 7 EIS spectra of as-prepared NR (a) and NP (b) arrays photoanodes

Table 2 Fitted values of equivalent circuit in PEC water splitting

Sample	R_s/ ($\Omega\cdot cm^2$)	R_1/ ($\Omega\cdot cm^2$)	CPE_1/ ($\mu F\cdot cm^{-2}$)
WO_3 NR	30.26	644.9	56.85
WO_3/Bi_2WO_6 NR	27.33	6195	82.12
$WO_3/BiVO_4$ NR	29.19	330.1	152.8
WO_3 NP	27.62	936.2	112.4
WO_3/Bi_2WO_6 NP	28.02	20235	49.62
$WO_3/BiVO_4$ NP	35.41	339.7	60.34

R_1 value, indicating the lowest resistance to charge transfer at the interface between $WO_3/BiVO_4$ photoanode and electrolyte solution. The EIS results conform to the LSV plots.

Besides, the efficiency of $WO_3/BiVO_4$ photoanodes in charge transfer was estimated according to $\eta_{trans}=J_{H_2O}/J_{Na_2SO_3}$, as shown in Fig. 8. The η_{trans} values at 1.23 V (vs RHE) of $WO_3/BiVO_4$ NR and NP photoanodes are 65.6% and 74.9%, respectively. It is speculated that the low values of η_{trans} result from the absence of cocatalyst on the surface of photoanode.

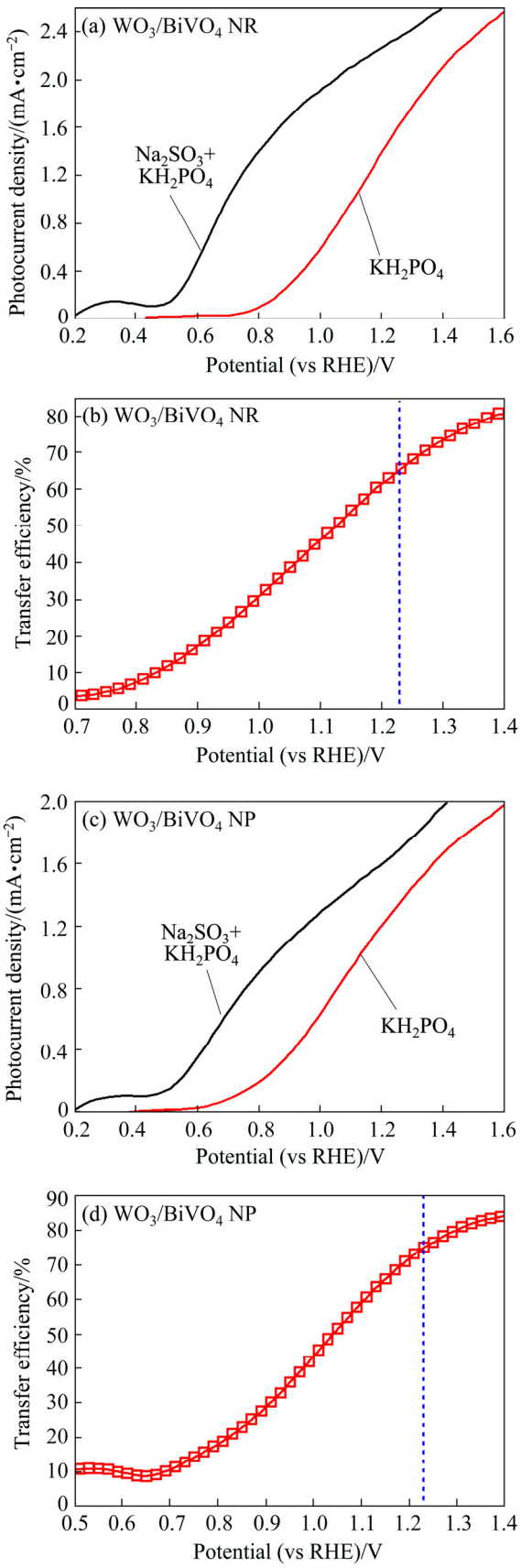

Fig. 8 Photocurrent density curves (a, c) in 0.5 mol/L Na_2SO_3 and KH_2PO_4 solution and surface charge transfer efficiency (b, d) of $BiVO_4/WO_3$ NR (a, b) and NP (c, d) arrays photoanodes

The PEC stability of $WO_3/BiVO_4$ photoanodes was evaluated at 1.23 V (vs RHE) under long-term irradiation, as shown in Fig. 9. The photocurrent density of $WO_3/BiVO_4$ photoanodes is stable and maintained about 90% after 2 h, indicating their excellent PEC stability in the water-splitting process.

In order to confirm the flat band potentials (V_{fb}) of the prepared photoanodes, Mott-Schottky (MS) plots were measured in darkness in a 0.5 mol/L KH_2PO_4 solution with applied frequencies of 1, 2.5 and 5 kHz, respectively. The V_{fb} and N_d could be estimated using the MS equation [33]:

$$\frac{1}{C^2}=\frac{2}{q\varepsilon\varepsilon_0 N_d}\left(V_E-V_{fb}-\frac{kT}{q}\right) \tag{3}$$

where C represents the specific capacitance, ε_0 indicates the permittivity of vacuum, ε denotes the dielectric constant of the electrode material used, q is the electron charge, V_E stands for the applied potential, N_d means the donor density, and k is the Boltzmann constant. As shown in Fig. 10, all M−S plots exhibit a positive slope, implying that the photoanode materials are n-type semiconductors. V_{fb} can be obtained from the intercept of the fitted tangent line. Compared with the WO_3 photoanode, $WO_3/BiVO_4$ photoanodes show a more negative V_{fb}, suggesting the possibility that the photogenerated electrons are transferred from $BiVO_4$ to WO_3 due to the more negative CB edge of $BiVO_4$.

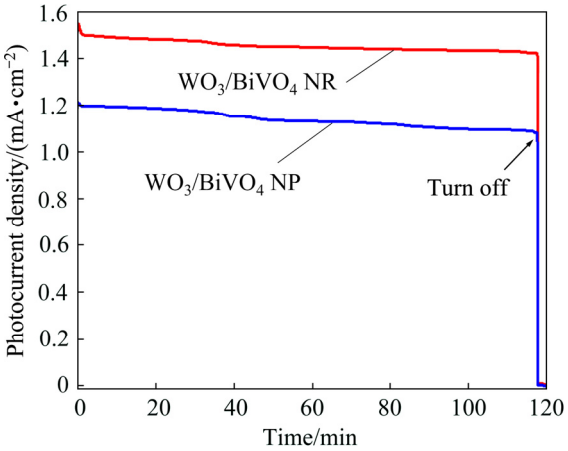

Fig. 9 Photocurrent density−time curve of $WO_3/BiVO_4$ NR and NP arrays photoanodes

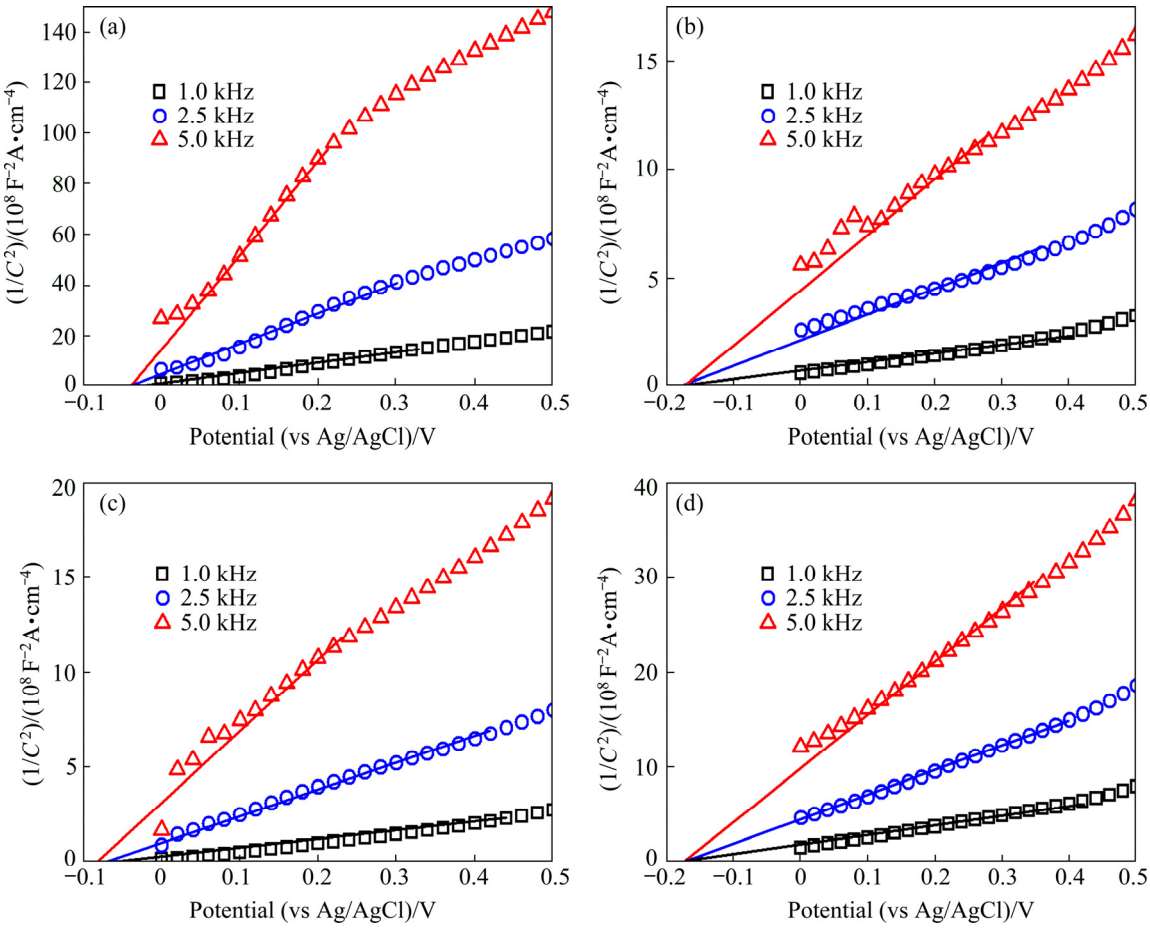

Fig. 10 MS plots of WO_3 NR (a), $WO_3/BiVO_4$ NR (b), WO_3 NP (c) and $WO_3/BiVO_4$ NP (d) arrays photoanodes

3.3 Mechanism of charge separation and transfer of $WO_3/BiVO_4$ photoanode

Figure 11 illustrates the mechanism of charge separation and transfer. With the phase transformation strategy applied, the dense $BiVO_4$ NS was coated on the WO_3 surface, thus forming a $WO_3/BiVO_4$ type-II heterojunction. Under irradiation, the electrons in $BiVO_4$ and WO_3 were excited from their valence band (VB) to the CB. Due to the more negative CB position of $BiVO_4$, the excited electrons in the CB of $BiVO_4$ were easily transferred to the CB of WO_3. These electrons were further moved onto the FTO substrate along the WO_3 NR and NP pathway and then to the Pt electrode through the external circuit. Then, the H^+ in the electrolyte reacted with the electrons to generate H_2 on the surface of Pt electrode. In the meantime, the photoexcited holes shifted from WO_3 to the VB of $BiVO_4$ and oxidized H_2O to produce oxygen on the $BiVO_4$ surface. Thus, type-II heterojunction can significantly improve the outcome of charge separation and transfer.

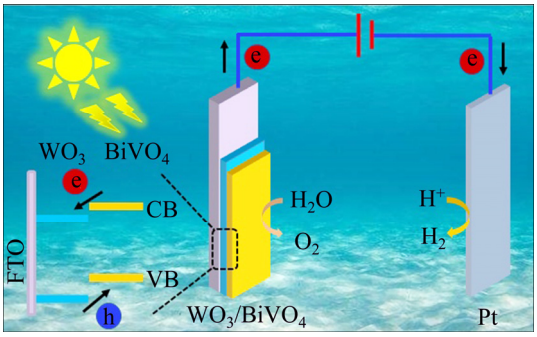

Fig. 11 Schematic illustration for charge separation and transfer of $WO_3/BiVO_4$ photoanode

4 Conclusions

(1) A versatile strategy of phase transformation was proposed to prepare $BiVO_4$ NS@WO_3 NR and NP arrays films. The strategy was carried out via a three-step hydrothermal process ($WO_3 \rightarrow WO_3/Bi_2WO_6 \rightarrow WO_3/BiVO_4$).

(2) As indicated by the SEM, TEM and XRD results, plenty of $BiVO_4$ NS successfully formed on the surface of the WO_3 NR and NP arrays films with Bi_2WO_6 NS as the intermediate product.

(3) The prepared $WO_3/BiVO_4$ photoanodes were applied for PEC water splitting and exhibited a significantly higher PEC activity compared with WO_3 photoanodes. It is believed that the proposed strategy is promising in the construction of various heterojunction systems for the future.

Acknowledgments

The authors are grateful for the financial supports from the National Natural Science Foundation of China (21808051, 51904356, 21703062).

References

[1] TURNER J A. Sustainable hydrogen production[J]. Science, 2004, 305(5686): 972−974.

[2] WAN Xiao-kang, WANG Lu, DONG Chung-li, MENENDEZ R G, HUANG Yu-cheng, MACCHIONI A, SHEN Shao-hua. Activating kläui-type organometallic precursors at metal oxide surfaces for enhanced solar water oxidation[J]. ACS Energy Letters, 2018, 3(7): 1613−1619.

[3] WANG S, LIU G, WANG L. Crystal facet engineering of photoelectrodes for photoelectrochemical water splitting[J]. Chemical Reviews, 2019, 119(8): 5192−5247.

[4] FUJISHIMA A, HONDA K. Electrochemical photolysis of water at a semiconductor electrode [J]. Nature, 1972, 238(5358): 37−38.

[5] CAO Guo-jian, CUI Bo, WANG Wen-qi, TANG Guang-ze, FENG Yi-cheng, WANG Li-ping. Fabrication and photodegradation properties of TiO_2 nanotubes on porous Ti by anodization [J]. Transactions of Nonferrous Metals Society of China, 2014, 24(8): 2581−2587.

[6] CAO Chang, XIE Xin-xin, ZENG Ya-mei, SHI Shao-hua, WANG Gui-zhen, YANG Liang, WANG Cai-zhuang, LIN Shi-wei. Highly efficient and stable p-type ZnO nanowires with piezotronic effect for photoelectrochemical water splitting [J]. Nano Energy, 2019, 61: 550−558.

[7] MAO Lian-lian, HUANG Yu-cheng, FU Yan-ming, DONG Chung-li, SHEN Shao-hua. Surface sulfurization activating hematite nanorods for efficient photoelectrochemical water splitting [J]. Science Bulletin, 2019, 64(17): 1262−1271.

[8] SOLTANI T, TAYYEBI A, HONG H, MIRFASIH M H, LEE B K. A novel growth control of nanoplates WO_3 photoanodes with dual oxygen and tungsten vacancies for efficient photoelectrochemical water splitting performance [J]. Solar Energy Materials and Solar Cells, 2019, 191: 39−49.

[9] YANG Ya-hui, XIE Ren-rui, LI Hang, LIU Can-jun, LIU Wen-hua, ZHAN Fa-qi. Photoelectrocatalytic reduction of CO_2 into formic acid using WO_{3-x}/TiO_2 film as novel photoanode [J]. Transactions of Nonferrous Metals Society of China, 2016, 26(9): 2390−2396.

[10] CHEN Yu-shiang, LIN Lu-yin. Novel synthesis of highly ordered $BiVO_4$ nanorod array for photoelectrochemical water oxidation using a facile solution process [J]. Journal of Power Sources, 2019, 436: 226842.

[11] CHANDRA D, SAITO K, YUI T, YAGI M. Tunable mesoporous structure of crystalline WO_3 photoanode toward efficient visible-light-driven water oxidation [J]. ACS Sustainable Chemistry & Engineering, 2018, 6(12): 16838−16846.

[12] ZHU T, CHONG M N, CHAN E S. Nanostructured tungsten trioxide thin films synthesized for photoelectrocatalytic water oxidation: A review [J]. ChemSusChem, 2014, 7(11): 2974−2997.

[13] APOLINÁRIO A, LOPES T, COSTA C, ARAÚJO J P, MENDES A M. Multilayered WO_3 nanoplatelets for efficient photoelectrochemical water splitting: The role of the annealing ramp [J]. ACS Applied Energy Materials, 2019, 2(2): 1040−1050.

[14] LIU Yang, LI Jie, LI Wen-zhang, YANG Ya-hui, LI Yao-min, CHEN Qi-yuan. Enhancement of the photoelectrochemical performance of WO_3 vertical arrays film for solar water splitting by gadolinium doping [J]. The Journal of Physical Chemistry C, 2015, 119(27): 14834−14842.

[15] BAI Shou-li, YANG Xiao-jun, LIU Cheng-yao, XIANG Xu, LUO Rui-xian, HE Jing, CHEN Ai-fan. An integrating photoanode of WO_3/Fe_2O_3 heterojunction decorated with NiFe-LDH to improve PEC water splitting efficiency [J]. ACS Sustainable Chemistry & Engineering, 2018, 6(10): 12906−12913.

[16] LI Hai-bin, ZHANG Jian, HUANG Guo-you, FU Sheng-hao, MA Chao, WANG Bai-yu, HUANG Qian-ru, LIAO Hong-wei. Hydrothermal synthesis and enhanced photocatalytic activity of hierarchical flower-like Fe-doped $BiVO_4$ [J]. Transactions of Nonferrous Metals Society of China, 2017, 27(4): 868−875.

[17] WANG Min, YANG Guang-jun, YOU Mei-yan, XIE Yuan-hua, WANG You-zhao, HAN Jin, ZHU Tong. Effects of Ni doping contents on photocatalytic activity of B-$BiVO_4$ synthesized through sol-gel and impregnation two-step method [J]. Transactions of Nonferrous Metals Society of China, 2017, 27(9): 2022−2030.

[18] GRIGIONI I, ABDELLAH M, CORTI A, DOZZI M. V, HAMMARSTROM L, SELLI E. Photoinduced charge-transfer dynamics in $WO_3/BiVO_4$ photoanodes probed through mid-IR transient absorption spectroscopy [J]. Journal of the American Chemical Society, 2018, 140(43): 14042−14045.

[19] SU J, GUO L, BAO N, GRIMES C A. Nanostructured $WO_3/BiVO_4$ heterojunction films for efficient photoelectrochemical water splitting [J]. Nano Letter, 2011, 11(5): 1928−1933.

[20] SHI X, Choi I Y, ZHANG K, KWON J, KIM D Y, LEE J K, OH S H, KIM J K, PARK J H. Efficient photoelectrochemical hydrogen production from bismuth vanadate-decorated tungsten trioxide helix nanostructures [J]. Nature Communications, 2014, 5: 4775.

[21] LEE M G, KIM D H SOHN W, MOON C W, PARK H, LEE S, JANG H W. Conformally coated $BiVO_4$ nanodots on porosity-controlled WO_3 nanorods as highly efficient type II heterojunction photoanodes for water oxidation [J]. Nano Energy, 2016, 28: 250−260.

[22] GAO Xue-hui, WU Hao-bin, ZHENG Ling-xia, ZHONG Yi-jun, HU Yong, LOU Xiong-wen. Formation of mesoporous heterostructured $BiVO_4/Bi_2S_3$ hollow discoids with enhanced photoactivity [J]. Angewandte Chemie, 2014, 126(23): 6027−6031.

[23] CHITRADA K C, GAKHAR R, CHIDAMBARAM D, ASTON E, RAJA K S. Enhanced performance of β-Bi_2O_3 by in-situ photo-conversion to Bi_2O_3−BiO_{2-x} composite photoanode for solar water splitting [J]. Journal of the Electrochemical Society, 2016, 163(7): H546−H558.

[24] LIU Can-jun, YANG Ya-hui, LI Wen-zhang, LI Jie, LI Yao-min, CHEN Qi-yuan. In situ synthesis of Bi_2S_3 sensitized WO_3 nanoplate arrays with less interfacial defects and enhanced photoelectrochemical performance [J]. Scientific Reports, 2016, 6: 23451.

[25] LIU Yang, WYGANT B R, KAWASHIMA K, MABAYOJE O, HONG T E, LEE S G, LIN Jie, KIM J H, YUBUTA K, LI Wen-zhang, LI Jie, MULLINS C B. Facet effect on the photoelectrochemical performance of a $WO_3/BiVO_4$ heterojunction photoanode [J]. Applied Catalysis B: Environmental, 2019, 245: 227−239.

[26] YANG Jiao, LI Wen-zhang, LI Jie, SUN Di-bo, CHEN Qi-yuan. Hydrothermal synthesis and photoelectrochemical properties of vertically aligned tungsten trioxide (hydrate) plate-like arrays fabricated directly on FTO substrates [J]. Journal of Materials Chemistry, 2012, 22(34): 17744−17752.

[27] HONG S J, LEE S, JANG J S, LEE J S. Heterojunction $BiVO_4/WO_3$ electrodes for enhanced photoactivity of water oxidation [J]. Energy & Environmental Science, 2011, 4(5): 1781−1787.

[28] XIA Li-gang, BAI Jing, LI Jin-hua, ZENG Qing-yi, LI Xue-jin, ZHOU Bao-xue. A highly efficient $BiVO_4/WO_3$/W heterojunction photoanode for visible-light responsive dual photoelectrode photocatalytic fuel cell [J]. Applied Catalysis B: Environmental, 2016, 183: 224−230.

[29] GRIGIONI I, CORTI A, DOZZI M V, SELLI E. Photoactivity and stability of $WO_3/BiVO_4$ photoanodes: effects of the contact electrolyte and of Ni/Fe oxyhydroxideprotection [J]. The Journal of Physical Chemistry C, 2018, 122(25): 13969−13978.

[30] MA Zi-zai, HOU Hui-lin, SONG Kai, FANG Zhi, WANG Lin, GAO Feng-mei, YANG Zuo-bao, TANG Bin, YANG Wei-you. Ternary WO_3/Porous-$BiVO_4$/FeOOH hierarchical architectures: Towards highly efficient photoelectrochemical performance [J]. ChemElectroChem, 2018, 5(23): 3660−3667.

[31] MA Zi-zai, SONG Kai, WANG Lin, GAO Feng-mei, TANG Bin, HOU Hui-lin, YANG Wei-you. $WO_3/BiVO_4$ type-II heterojunction arrays decorated with oxygen-deficient ZnO passivation layer: A highly efficient and stable photoanode [J]. ACS Applied Materials & Interfaces, 2018, 11(1): 889−897.

[32] XU Shang, FU Ding-fa, SONG Kai, WANG Lin, YANG Zuo-bao, YANG Wei-you, HOU Hui-lin. One-dimensional $WO_3/BiVO_4$ heterojunction photoanodes for efficient photoelectrochemical water splitting [J]. Chemical Engineering Journal, 2018, 349: 368−375.

[33] LIU Can-jun, YANG Ya-hui, LI Jie, CHEN Shu. Phase transformation synthesis of TiO_2/CdS heterojunction film with high visible-light photoelectrochemical activity [J]. Nanotechnology, 2018, 29(26): 265401.

一种通用的相转换策略构建 $BiVO_4$ 纳米薄片@WO_3 阵列异质结光阳极

苏 昕[1]，刘灿军[1]，刘 洋[2]，杨亚辉[3]，刘 玄[1]，陈 述[1]

1. 湖南科技大学 化学化工学院 理论有机化学与功能分子教育部重点实验室，湘潭 411201；
2. 中南大学 化学化工学院，长沙 410083；
3. 湖南师范大学 化学化工学院，长沙 410081

摘 要：提出一种制备 $BiVO_4$ 纳米薄片@WO_3 纳米棒和纳米片薄膜的相转换策略。这种策略包括三步水热过程(WO_3→WO_3/Bi_2WO_6→$WO_3/BiVO_4$)。表征结果表明：大量的 $BiVO_4$ 纳米薄片原位生长在 WO_3 纳米棒和纳米片阵列薄膜表面，从而形成 $WO_3/BiVO_4$ 异质结。制备的 $WO_3/BiVO_4$ 异质结薄膜作为光阳极被用于光电化学分解水，并展现出优异的光电化学活性。在可见光照射和没有沉积助催化剂的情况下，$WO_3/BiVO_4$ 纳米棒和纳米片光阳极的光电流密度分别达到约 1.56 和 1.20 mA/cm^2(V=1.23 V (vs RHE))。

关键词：光阳极；钒酸铋；氧化钨；异质结

(Edited by Xiang-qun LI)